Journal of Photonics for Energy

PhotonicsforEnergy.SPIEDigitalLibrary.org

# Enhanced photovoltaic performance of inverted hybrid bulk-heterojunction solar cells using $TiO_2$/reduced graphene oxide films as electron transport layers

Andreia Morais
João Paulo C. Alves
Francisco Anderson S. Lima
Monica Lira-Cantu
Ana Flavia Nogueira

SPIE.

Downloaded From: http://photonicsforenergy.spiedigitallibrary.org/ on 04/20/2016 Terms of Use: http://spiedigitallibrary.org/ss/TermsOfUse.aspx

# Enhanced photovoltaic performance of inverted hybrid bulk-heterojunction solar cells using $TiO_2$/reduced graphene oxide films as electron transport layers

**Andreia Morais,[a] João Paulo C. Alves,[a] Francisco Anderson S. Lima,[b] Monica Lira-Cantu,[b] and Ana Flavia Nogueira[a,*]**

[a]University of Campinas (UNICAMP), Chemistry Institute, PO Box 6154, Campinas-SP 13083-970, Brazil

[b]Autonomous University of Barcelona (UAB), Catalan Institute of Nanocience and Nanotechnology (ICN2), Building ICN2, Bellaterra, Barcelona E-0193, Spain

**Abstract.** In this study, we investigated inverted hybrid bulk-heterojunction solar cells with the following configuration: fluorine-doped tin oxide (FTO) $|TiO_2/RGO|P3HT:PC_{61}BM|V_2O_5$ or PEDOT:PSS|Ag. The $TiO_2$/GO dispersions were prepared by sol-gel method, employing titanium isopropoxide and graphene oxide (GO) as starting materials. The GO concentration was varied from 0.1 to 4.0 wt%. The corresponding dispersions were spin-coated onto FTO substrates and a thermal treatment was performed to remove organic materials and to reduce GO to reduced graphene oxide (RGO). The $TiO_2$/RGO films were characterized by x-ray diffraction, Raman spectroscopy, and microscopy techniques. Atomic force microscopy (AFM) images showed that the addition of RGO significantly changes the morphology of the $TiO_2$ films, with loss of uniformity and increase in surface roughness. Independent of the use of $V_2O_5$ or PEDOT: PSS films as the hole transport layer, the incorporation of 2.0 wt% of RGO into $TiO_2$ films was the optimal concentration for the best organic photovoltaic performance. The solar cells based on $TiO_2$/RGO (2.0 wt%) electrode exhibited a ~22.3% and ~28.9% short circuit current density ($J_{sc}$) and a power conversion efficiency enhancement, respectively, if compared with the devices based on pure $TiO_2$ films. Kelvin probe force microscopy images suggest that the incorporation of RGO into $TiO_2$ films can promote the appearance of regions with different charge dissipation capacities. © *2015 Society of Photo-Optical Instrumentation Engineers (SPIE)* [DOI: 10.1117/1.JPE.5.057408]

**Keywords:** nanocomposites; reduced graphene oxide; titanium oxide; inverted solar cells; vanadium oxide; electron transport layer.

Paper 14093SSP received Nov. 5, 2014; accepted for publication Feb. 16, 2015; published online Mar. 12, 2015.

## 1 Introduction

Inverted hybrid bulk-heterojunction solar cells based on conjugated polymers and fullerene derivatives have attracted much attention because of their numerous advantages. These devices are considered promising candidates as renewable energy sources because of their low weight, low cost, stability and simple fabrication for large area processing.[1] These solar cells occupy a prominent position in the context of photovoltaic devices for solar energy conversion into electricity. This position is due to recent progress which allowed a significant increase in power conversion efficiency (PCE) of these cells, reaching nearly 10% over the last years.[2–4] Additional understanding of the interfaces involved in the inverted hybrid bulk-heterojunction solar cells is needed and thus, the development of new materials becomes crucial to further improve the efficiency of these devices.

*Address all correspondence to: Ana Flavia Nogueira, E-mail: anaflavia@iqm.unicamp.br

1947-7988/2015/$25.00 © 2015 SPIE



Downloaded From: http://photonicsforenergy.spiedigitallibrary.org/ on 04/20/2016 Terms of Use: http://spiedigitallibrary.org/ss/TermsOfUse.aspx

Currently, there is a great interest in developing new materials to act as the electron transport layer (ETL) between the active layer and the conductive substrate in these devices.[1] The main requirements for a given film to act as ETL involve high electron mobility and transparency in the visible region in order to allow transmission of light into the active layer. These requirements limit the choice to a few materials that have these characteristics, among which are the well-known and widely used titanium oxide ($TiO_2$)[5,6] and zinc oxide (ZnO).[7,8] These materials also exhibit good compatibility with the lowest unoccupied molecular orbital energy level for the majority of polymers used and act as hole blocking layers preventing a short circuit in the device.

The use of $TiO_2$ films as ETL is advantageous due to their low toxicity, transparency, facile fabrication and well-known physical and chemical stability. In general, thin $TiO_2$ films have been introduced as ETL because of their large bandgap (3.7 eV) and well-matched energy levels (valence band of ~8.1 eV and conduction band of ~4.4 eV). Thus, these films facilitate the electron injection and transport; and at the same time, block the hole collection at the cathode.[9] However, the slow charge carrier diffusion in a $TiO_2$ film increases the probability for charge recombination, resulting in decreased energy conversion efficiency of the solar cells. The promising alternative to improve the electronic transport is the incorporation of carbonaceous materials, such as carbon nanotubes (CNTs),[10] graphene, and their derivatives,[11,12] into $TiO_2$ films. In a recent work, Zhang et al.[10] proposed the incorporation of CNTs in $TiO_2$ films to act as ETL in solar cells with the following configuration: ITO|$TiO_2$/CNTs|P3HT:$PC_{61}$BM|$MoO_3$|Al. In this work, they demonstrated that the conversion efficiency for these devices practically doubles with the addition of a small amount of CNTs (0.1 wt%). This influence was closely associated with the amount of CNTs. In addition, the devices assembled with $TiO_2$/multiwalled carbon nanotube (MWCNT) or $TiO_2$/single-walled carbon nanotube films showed similar photovoltaic behavior. In this context, due to the electron-accepting ability presented by these carbonaceous materials, there is also an interest in their use with the aim of improving the electron transport properties in semiconductor films.[13]

Graphene, a single layer of $sp^2$-bonded carbon atoms tightly packed into a two-dimensional honeycomb structure, has attracted a lot of attention since its isolation in 2004, because of its outstanding mechanical, thermal, optical, and electrical properties.[14] Various methods have been developed for the preparation of graphene, including micromechanical exfoliation,[15] epitaxial growth,[16] electrochemical exfoliation of graphite in ionic liquids,[17] and the chemical modification of graphite.[18] The latter method was proven to be an effective, inexpensive method and was often applied in large-scale production of this material. In this case, the graphene oxide (GO) product is an electrically insulating material and usually possesses a rich assortment of oxygen-containing groups such as carboxyl, hydroxyl, carbonyl, and epoxy groups.[19] However, the GO sheets can be reduced by several methods[20–23] in order to increase their electrical conductivity by the partial restoration of the $sp^2$-hybridized network. In general, the resulting product, also known as reduced graphene oxide (RGO), has properties similar to graphene, although the reduction methods do not fully restore the ideal characteristics of graphene sheets.[14] Due to its high surface area, transparency and its electron-accepting properties, RGO is a good material to enhance the charge carrier transport in semiconductors films, and consequently to improve the performance of the devices.[24]

According to other reports, $TiO_2$/RGO nanocomposites have been widely investigated in photovoltaic devices,[25] photocatalysts,[26,27] and lithium-ion batteries.[28] Recently, in the field of dye-sensitized solar cells (DSSC), graphene and its derivatives were employed as counter electrodes[29,30] and $TiO_2$/RGO nanocomposites were used as a photoanode to improve the DSSC performance.[31–33] Currently, there is an interest in using these nanocomposites as films to act as ETL in organic solar cells. In two recent works, Zhang et al.[11,12] proposed the use of thin $TiO_2$/RGO films as ETL in inverted solar cells with the following configurations: ITO|$TiO_2$/RGO|P3HT:$PC_{61}$BM|$MoO_3$|Ag or ITO| and $TiO_2$/RGO|P3HT:$PC_{61}$BM|PEDOT:PSS|Ag. They reported that solar cells based on these composite films exhibit an improvement in the current density and also in the energy conversion efficiency. Impedance measurements revealed that the $TiO_2$/RGO composite films as ETL could efficiently reduce the charge recombination and increase the electron lifetime. Although the advantages of RGO sheet incorporation in any $TiO_2$ matrix are widely disseminated, a detailed explanation of the photovoltaic activity of these nanocomposites, as well the role of graphene and its derivatives is still very controversial and scarce in the literature. For this



Downloaded From: http://photonicsforenergy.spiedigitallibrary.org/ on 04/20/2016 Terms of Use: http://spiedigitallibrary.org/ss/TermsOfUse.aspx

reason, there is a need for further studies to improve the general understanding of the photovoltaic behavior when carbonaceous materials are used.

In this work, RGO was incorporated in $TiO_2$ films to be used as ETL in inverted hybrid bulk-heterojunction solar cells aiming to decrease the charge recombination and to increase the energy conversion efficiency. The solar cells were assembled with the following configuration: FTO|$TiO_2$ or $TiO_2$/RGO|P3HT:$PC_{61}BM$|$V_2O_5$|Ag. Compared to the solar cell using only $TiO_2$ as ELT, we observed that the incorporation of RGO (2.0 wt%) in the $TiO_2$ film showed an increase of 22.3% in $J_{sc}$ and hence an improvement in the conversion efficiency. In this case, independent of the use of $V_2O_5$ or PEDOT:PSS films as the hole transport layer (HTL), the effect was positive after adding 2.0 wt% of RGO into the $TiO_2$ film. Kelvin probe force microscopy (KPFM) images suggest that the incorporation of RGO into $TiO_2$ film promotes the appearance of regions with different charge dissipation capacity. In others words, because of its conductive properties, the RGO can act as an electron collector in the $TiO_2$ film, which facilitates a rapid electron transport resulting in an increase in photocurrent and conversion efficiency.

## 2 Experimental Methods

### 2.1 *Materials*

All reagents were of analytical grade and used without further purification. The natural graphite powder was purchased from Nacional de Grafite LTDA (code: Micrograf 99507 UJ). Poly(3-hexylthiophene) (P3HT) (regioregular, Merck®, 98%) was used as the electron donor material, and [6,6]-phenyl-$C_{61}$-butyric acid methyl ester ($PC_{61}BM$) (Solenne BV, 99.5%) was used as the electron acceptor material in the inverted solar cells. All other reagents were purchased from Sigma–Aldrich. The fluorine-doped tin oxide (FTO) conductive substrates were supplied by SOLEMS (sheet resistance: 70 to 100 $\Omega\,sq^{-1}$). The substrates were cleaned with water-detergent solution, deionized water and ethanol (99%) successively in ultrasonic baths for 15 min. All substrates were dried with compressed nitrogen and were treated in the UV surface decontamination system (Novascan, PSD-UV) connected to the oxygen supply for 20 min.

### 2.2 *Synthesis of GO*

GO was synthesized from natural graphite powder using a modified Hummers and Offeman's method.[34] The graphite powder (10 g) was added to a mixture of concentrated $H_2SO_4$ (60 mL), $K_2S_2O_8$ (5 g) and $P_2O_5$ (5 g). The solution was heated to 80°C in an oil bath and was stirred for 6 h. The mixture was then carefully diluted with distilled water, filtered, and washed until the rinse water pH turned neutral. The product was dried in air at ambient temperature overnight. The preoxidized graphite powder was added to a mixture of concentrated $H_2SO_4$ (200 mL) and $NaNO_3$ (5 g) under vigorous stirring, and the solution was cooled to 0°C. Next, 15 g of $KMnO_4$ was added gradually under stirring and the temperature of the mixture was kept below 20°C. The mixture was stirred at 40°C for 4 h, and then diluted with distilled water (2 L) in an ice bath. The reaction was terminated by the addition of 30% (v/v) $H_2O_2$ solution (50 mL) and a brilliant yellow product was formed along with bubbling. The mixture was filtered and washed with 3% (v/v) $H_2SO_4$ solution in order to remove metal ions. The GO product was suspended in distilled water to give a viscous and brown dispersion, which was subjected to dialysis to completely remove metal ions and acids. The resulting GO dispersion (1.8% w/w) was used in the preparation of thin $TiO_2$/RGO films.

### 2.3 *Preparation of Thin $TiO_2$/RGO Film*

Initially, the water present in the GO dispersion was removed to avoid immediate hydrolysis and condensation of the titanium isopropoxide [$Ti(O^i Pr)_4$], which is the precursor of $TiO_2$. In this case, the solvent exchange was carried out as follows: an aliquot (~420 mg) of the aqueous GO dispersion (1.8% w/w) was dispersed first in ethanol and then diethyl ether was added, in a ratio of 1:5 (v/v). The GO precipitates due to the addition of a bad solvent (diethyl ether). After



Downloaded From: http://photonicsforenergy.spiedigitallibrary.org/ on 04/20/2016 Terms of Use: http://spiedigitallibrary.org/ss/TermsOfUse.aspx

removing the supernatant by centrifugation, the solvent exchange procedure was repeated to ensure complete removal of water. Evaporation of the solvent was carried out in a vacuum oven. The dry GO was redispersed in ethanol (3.0 mL) using an ultrasonic bath and then acetylacetone (140 $\mu$L) and $Ti(O^i Pr)_4$ (200 $\mu$L) were added to the dispersion. The brown dispersion was designated as $TiO_2$/GO (4.0 wt%). The dispersion containing only $TiO_2$ was also prepared from a mixture of $Ti(O^i Pr)_4$ (200 $\mu$L), acetylacetone (140 $\mu$L) and ethanol (3.0 mL). Other dispersions as $TiO_2$/GO (2.0 wt%), $TiO_2$/GO (1.0 wt%), $TiO_2$/GO (0.5 wt%), and $TiO_2$/GO (0.1 wt%) were prepared by dilution of the $TiO_2$/GO (4.0 wt%) using the dispersion containing only $TiO_2$ as the diluent. The $TiO_2$ and $TiO_2$/GO dispersions were deposited on the FTO substrates by spin-coating followed by thermal treatment at 350°C for 1 h with a heating rate of 10°C $min^{-1}$. This thermal treatment step is very important to remove the organic materials and also to reduce GO to RGO, which is a more conductive material than GO. The resulting films, with a thickness around 30 to 60 nm as estimated by the scanning electron microscopy (SEM) images (see Fig. 13 in Appendix), were transparent and uniform without any noticeable cracks. All the nanocomposite films were denominated as $TiO_2$/RGO.

## 2.4 *Characterization*

X-ray diffraction measurements were performed directly on the samples of GO, RGO, $TiO_2$ and $TiO_2$/RGO films using a Shimadzu XRD 7000 diffractometer (40 kV, 30 mA) with Cu ($\lambda = 1.541\,78$ Å) irradiation in the $2\theta$ range of 5 to 80 deg. The Raman spectra of the samples were obtained in a confocal Raman spectrometer (model T64000, Jobin Yvon, USA), equipped with a charge coupled device detector and an Olympus BTH 2 microscope. The excitation laser was set at 514 nm with a 20-fold magnification objective lens. The thermal stability of the lyophilized GO sample was analyzed on TA Instruments 2950 thermogravimetric analyzer at a heating rate of 10°C $min^{-1}$, using a synthetic air stream (100 $dm^3\,min^{-1}$) in the temperature range of 50°C to 1000°C and the average sample weight was within the range of 3 to 5 mg.

A Thermo VG Scientific Sigma Probe instrument was used to carry out the x-ray photoelectron spectroscopy (XPS) analysis of the GO and RGO (350°C for 1 h) films. The monochromatic Al K$\alpha$ x-ray source (1486.6 eV) was focused on the sample (400 $\mu m^2$ size). The high resolution spectra were collected with a pass energy of 20 eV and an energy step size of 0.1 eV with the flood gun turned on to eliminate any surface charge. $TiO_2$ and $TiO_2$/RGO films deposited onto FTO substrates were characterized by atomic force microscopy (AFM) and KPFM analysis. AFM and KPFM measurements were obtained simultaneously using a NX10 Atomic Force Microscope from Park Systems in the tapping mode with a three lock-in module. The KPFM images were obtained in dry atmosphere and an electrical frequency of 17 kHz with an amplitude of 5 V was used. A Pt/Ir-coated tip with a mechanical resonance frequency of 75 kHz and a force constant of 2.8 N $m^{-1}$ was used.

Optical microscopy images were taken with a Nikon Eclipse 5i (H5505, Nikon, Japan) microscope equipped with Digital Sight Camera System (DS-Fi1 Nikon, Japan) and using an objective lens with a magnification of $4\times/0.10$. The optical absorption spectra of the $TiO_2$ and the $TiO_2$/RGO films were measured by using a Varian spectrophotometer, model Cary 5G UV-VIS, NIR, with a diffuse reflectance accessory. Measurements were carried out within the range of 300 to 800 nm, using Teflon as a reference material for all samples.

## 2.5 *Fabrication of Photovoltaic Devices*

In this work, we fabricated inverted hybrid bulk-heterojunction solar cells with the following configuration: FTO|$TiO_2$/RGO|P3HT:$PC_{61}$BM|$V_2O_5$|Ag. First, solutions of P3HT and $PC_{61}$BM were prepared with 1:1 ratio and the total concentration of P3HT:$PC_{61}$BM was 60 mg $mL^{-1}$ in chlorobenzene. On the FTO substrates coated with thin $TiO_2$ and $TiO_2$/RGO films, the P3HT:$PC_{61}$BM solution was spin-coated at 1000 rpm and the thickness of the active layer was about 200 nm. The films were annealed at 150°C for 15 min in an $N_2$-filled glove box. The $V_2O_5$ hydrate solution was obtained using the procedure described in the literature.[35] In this case, a 1:1 mixture of $V_2O_5$ hydrate (9 mg $mL^{-1}$) in isopropanol was spin-coated at 3000 rpm on the FTO|$TiO_2$ or $TiO_2$/RGO|P3HT:$PC_{61}$BM and then annealed at 150°C



Downloaded From: http://photonicsforenergy.spiedigitallibrary.org/ on 04/20/2016 Terms of Use: http://spiedigitallibrary.org/ss/TermsOfUse.aspx

for 15 min in an $N_2$-filled glove box. A 100-nm thick Ag back metal electrode was deposited by thermal evaporation in an evaporation system (Auto 306, Boc Edwards) with a base pressure of $10^{-7}$ torr at the deposition rate of 1.0 Å $s^{-1}$. The final active area was 0.17 $cm^{-2}$. The configuration of the devices (FTO|$TiO_2$/RGO|P3HT:$PC_{61}$BM|$V_2O_5$|Ag) and the chemical structures of P3HT and $PC_{61}$BM are shown in Fig. 1.

For other the configuration (FTO|$TiO_2$/RGO|P3HT:$PC_{61}$BM|PEDOT:PSS|Ag), the PEDOT:PSS layer was spin-coated at 5000 rpm over the active layer (FTO|$TiO_2$/RGO|P3HT:$PC_{61}$BM). The PEDOT:PSS commercial solution was modified by the addition of the surfactant (Zonyl FS300) with a ratio of Zonyl : PEDOT:PSS equal to 0.5% w/w. The films were annealed at 150°C for 15 min in an $N_2$-filled glove box. A 100-nm thick Ag back metal electrode was deposited by thermal evaporation as described previously.

### 2.6 *Photovoltaic Characterization*

The solar simulation was performed on a KHS1200 (Steuernagel Solarkonstant) equipped with an AM1.5 filter for all characterizations (100 mW $cm^{-2}$, AM1.5G). The equipment was calibrated according to the ASTM G173 standard. *J–V* curves were measured using a Keithley 2601 multimeter. The light intensity was calibrated to 100 mW $cm^{-2}$ with a Zipp&Konen CM-4 pyranometer, which was used constantly during measurements to set the light intensity, and a calibrated S1227-1010BQ photodiode from Hamamatsu was also used for calibration before each measurement. Incident photon-to-current conversion efficiency (IPCE) analyses were done with a QE/IPCE measurement System from Oriel (from 300 to 700 nm; at 10 nm intervals). The results were not corrected for any intensity losses due to light absorption or reflection by the glass substrates.

## 3 Results

### 3.1 *Morphological and Structural Characterization of the GO and RGO Films*

The GO and RGO films were characterized through x-ray diffraction and Raman spectroscopy, and the results are shown in Figs. 2(a) and 2(b), respectively.

According to Fig. 2(a), the XRD diffraction pattern of the GO film exhibits a peak at $2\theta = 10.7°$ corresponding to an interplanar spacing of $d(002) = 8.3$ Å. Other diffraction peaks correspond to the crystalline phases of the FTO conductive substrate, and these are marked with asterisks (*). The increased interplanar distance from the characteristic peak of graphite (3.35 Å) is related to the presence of oxygen-containing functional groups and water molecules introduced into the carbon lattice during the oxidation.[36] When the GO film is heat-treated at 350°C for 1 h, the $2\theta$ peak at 10.7° disappears and a broader and weaker peak centered at around $2\theta = 21.5°$ with a interplanar spacing of $d(002) = 4.1$ Å is observed. This implies that the oxygen-containing functional groups of GO were partially removed through thermal treatment and without adding any reducing agent.[37] There is also a noticeable decrease in the intensity of the diffraction peak due to the loss of crystallinity of the material, with the formation of more disordered, less packed structures.

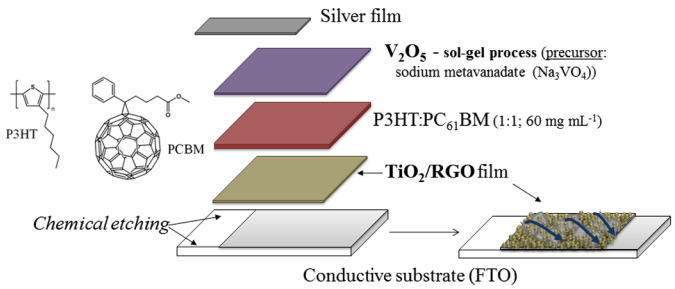


**Fig. 1** Representation of the inverted solar cell assembled with the following configuration: FTO|$TiO_2$/RGO|P3HT:$PC_{61}$BM|$V_2O_5$|Ag. Chemical structures of the P3HT and the $PC_{61}$BM.



Downloaded From: http://photonicsforenergy.spiedigitallibrary.org/ on 04/20/2016 Terms of Use: http://spiedigitallibrary.org/ss/TermsOfUse.aspx

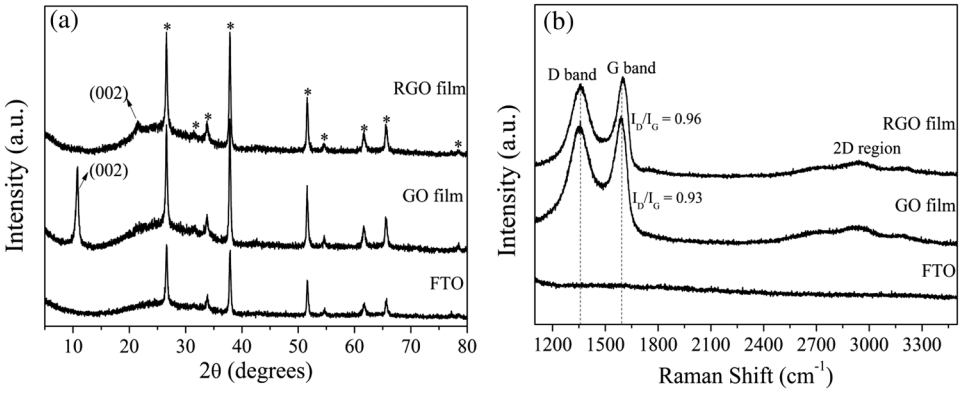


**Fig. 2** (a) X-ray diffraction patterns and (b) Raman spectra for FTO substrate, GO, and RGO (350°C for 1 h) films.

The Raman spectra [Fig. 2(b)] of the GO and RGO films exhibit three vibrational modes at 1360, 1600 and 2700 $cm^{-1}$, corresponding to the D, G and 2-D bands, respectively. The G band is related to the $E_{2g}$ vibration mode of the $sp^2$ carbon domains and it can be used to ascertain the degree of graphitization, whereas the D band is associated with structural defects and partially disordered structures of the $sp^3$ domains. The 2-D band is the second order of the D band and its frequency is generally used to quantify the number of graphene layers and stacking order in few-layers graphene.[38,39] The intensity ratio between the D and G bands ($I_D/I_G$) is often used as a parameter to correlate the disorder degree in the carbonaceous structures.[38] In this case, the $I_D/I_G$ ratio was 0.93 for the GO film and 0.96 for the RGO film. This small change suggests that a decrease in the average size of the $sp^2$ domains formed during the thermal treatment at 350°C for 1 h. It is reasonable to consider that the reduction of GO causes fragmentation along the reactive sites and yields new graphitic domains, which led to the RGO sheets being smaller but more numerous. The small size of the RGO sheets will result in a large number of edges. The edges will act as defects. This explains the presence of the D band, with considerable intensity, even after the thermal reduction of GO.[40,41] Furthermore, the thermal treatment at 350°C for 1 h promoted the partial removal of the labile oxygen-containing functional groups, as proposed in the thermogravimetric analysis (TGA) curve obtained for the lyophilized GO sample (see Fig. 13 in Appendix).[42]

XPS was used to determine the chemical composition of the GO and RGO (350°C for 1 h) films. XPS survey spectra (up to 1000 eV) were obtained to identify and quantify the elements and chemical groups present in these samples, as shown in Fig. 14 (see in Appendix). The spectra essentially showed the presence of the elements carbon (C1s) and oxygen (O1s) in the region around 284 and 532 eV, respectively. Table 3 (see in Appendix) details the atomic percentages found in these samples. In the RGO film, the C percentage was 85.2 at% (and 14.8 at% of O), compared to 67.0 at% (and 33.0 at% of O) in the GO film. This is an indication that the oxygen-containing functional groups have been partially removed after the thermal treatment at 350°C for 1 h. High resolution XPS C1s spectra obtained for these films are shown in Fig. 3.

The XPS C1s peak of the GO film [Fig. 3(a)] can be decomposed into seven components which correspond to the following functional groups: $sp^2$-hybridized carbon (C═C, 284.2 eV), $sp^3$-hybridized carbon (C─C, 284.9 eV), hydroxyl/phenols (C─OH, 285.5 eV), epoxy/ether (C─O─C, 286.4 eV), carbonyl (C═O, 287.7 eV), carboxyl (O─C═O, 288.7 eV) groups and a shake-up satellite peak ($\pi \rightarrow \pi*$, 289.8 eV), characteristic of aromatic C structures.[43–45] The XPS C1s analysis suggests that the GO film contains a large number of functional groups on its surface such as epoxy, carbonyl, hydroxyl, and carboxyl groups. The XPS spectrum of the RGO film [Fig. 3(b)] shows that the same peaks are related to the oxygen containing functional groups, however, they are much less intense. Through this analysis, it was possible to demonstrate the presence of oxygen functional groups on the surface even after a reduction process by thermal treatment at 350°C for 1 h, indicating that the GO film was not fully reduced. However, it was sufficient to increase the aromatic character of the material, turning RGO into a more conductive material than the GO.[40,46–48] Another interesting fact can be evidenced in Table 4 (see Appendix) where the concentration of C═C bonds (~53%) found in the RGO film is larger than



Downloaded From: http://photonicsforenergy.spiedigitallibrary.org/ on 04/20/2016 Terms of Use: http://spiedigitallibrary.org/ss/TermsOfUse.aspx

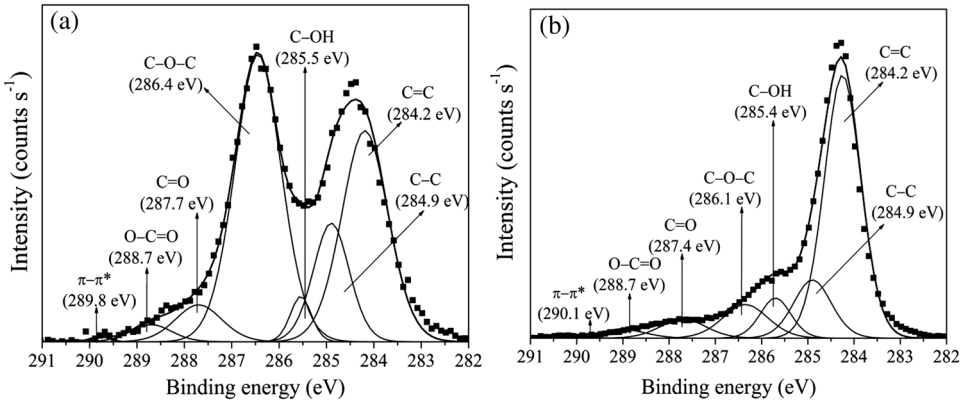


**Fig. 3** XPS spectrum of the carbon region (C1s) for (a) GO and (b) RGO (350°C for 1 h) films.

the GO film (~32%). This is another evidence of almost complete restoration of the $sp^2$-hybridized network in the RGO film after thermal treatment.

### 3.2 *Morphological and Structural Characterization of the $TiO_2$/RGO Films*

Figure 4 exhibits the XRD diffraction pattern and the Raman spectra of the FTO substrate, $TiO_2$, $TiO_2$/RGO (2.0 wt%) films and $TiO_2$/RGO (2.0 wt%) powder when subjected to thermal treatment at 350°C for 1 h.

The crystal planes corresponding to the titanium oxide were not observed directly in the XRD diffraction pattern in Fig. 4(a). This can be due to the overlap from other diffraction peaks that correspond to crystalline phases of the FTO substrate [marked with asterisks (*)]. The x-ray diffraction patterns obtained for the $TiO_2$/RGO (2.0 wt%) powder exhibit a good crystallinity. The peaks at 2θ values of 25.2, 37.8, 47.9, 53.9, 55.1, 62.6, 68.9, 70.2 and 75.2 deg can be indexed to (101), (004), (200), (105), (211), (204), (220), (116), and (215) planes of anatase titania, respectively. No diffraction peak was detected for the carbon species in the films, due to both the low concentration and the low relative intensity of the main diffraction peak for RGO [see Fig. 2(a)]. However, the Raman spectra [Fig. 4(b)] showed wide and less intense bands vibrations in the region between 300 and 800 $cm^{-1}$ which are associated with the titanium oxide. In the $TiO_2$/RGO (2.0 wt%) film, the presence of RGO was confirmed with the appearance of three vibrational modes at 1358, 1607 and 2690 $cm^{-1}$ related to D, G and 2-D bands, respectively. The $I_D/I_G$ ratio around 1.0 suggests a relative increase in structural disorder in relation to the film containing only RGO ($I_D/I_G = 0.96$), possibly because of the interaction between the RGO sheets and $TiO_2$ nanoparticles.

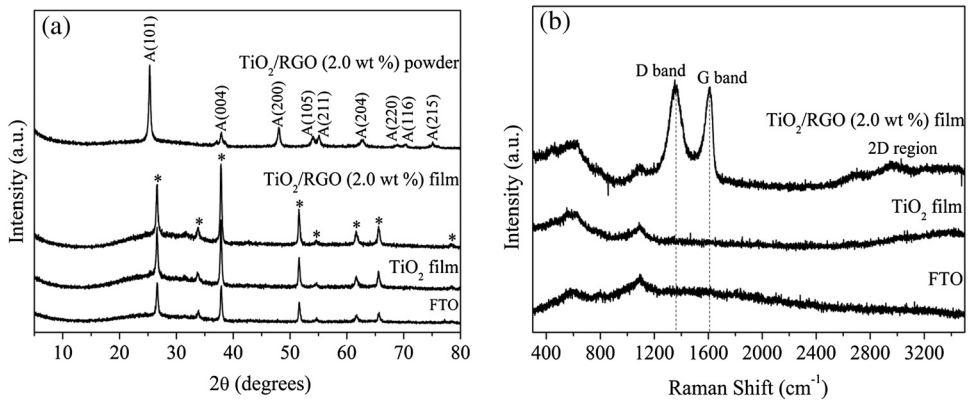


**Fig. 4** (a) X-ray diffraction patterns for FTO substrate, $TiO_2$, $TiO_2$/RGO (2.0 wt%) films, and $TiO_2$/RGO (2.0 wt%) powder. (b) Raman spectra for FTO substrate, $TiO_2$, and $TiO_2$/RGO (2.0 wt%) films.



Downloaded From: http://photonicsforenergy.spiedigitallibrary.org/ on 04/20/2016 Terms of Use: http://spiedigitallibrary.org/ss/TermsOfUse.aspx

Optical microscopy images (Fig. 5) of the $TiO_2$, $TiO_2$/RGO (0.1 wt%), $TiO_2$/RGO (0.5 wt%), $TiO_2$/RGO (1.0 wt%), $TiO_2$/RGO (2.0 wt%), and $TiO_2$/RGO (4.0 wt%) films were obtained in order to evaluate how the RGO sheets are distributed throughout the $TiO_2$ film.

In this case, the RGO sheets are well distributed throughout the composite films, probably on the surface, independent of the RGO concentration. In addition, the size and shape of the RGO sheets vary widely for all the $TiO_2$/RGO films. The increased surface roughness of the composite films with increasing RGO concentration was also observed through these images. The $TiO_2$/RGO (4.0 wt%) film [Fig. 5(f)], for example, shows many regions with agglomerations of the RGO sheets providing a rougher appearance compared to the other composite films. Another important factor to be considered is the thickness of the $TiO_2$ and $TiO_2$/RGO films, estimated in this work through SEM images obtained by the cross-section of all films.

Figure 13 (see in Appendix) illustrates a graph relating thickness variation versus the concentration of RGO (%) for each film. This graph shows that the thickness increased significantly from 32.2 to 58.5 nm when the concentration of RGO ranged from 0 to 1.0 wt%. At higher RGO concentrations, the thickness has not changed significantly. The $TiO_2$/RGO (4.0 wt%) film, for example, presented a thickness of about 61 nm, which is relatively close to the value measured for the $TiO_2$/RGO (1.0 wt%) film (~58.3 nm). The increased thickness of the films is directly related to the increased viscosity of the $TiO_2$ dispersions due to the addition of GO. In general, these features, such as roughness and thickness, influence the performance of the photovoltaic devices.

In order to investigate the morphological effect of the introduction of RGO in $TiO_2$ films, AFM images were obtained and presented in Fig. 6. The AFM image shows that the FTO substrate has a surface roughness around 7.6 nm and a homogeneous size distribution and grain shape. The film containing only $TiO_2$ has a low surface roughness (RMS $= 3.5 \pm 0.1$ nm). The decrease in roughness is related to coating of the FTO substrate by the thin $TiO_2$ film. The addition of RGO significantly changes the morphology of the $TiO_2$ films, with loss of uniformity and increase in surface roughness. With the addition of RGO (2.0 wt%) and (4.0 wt%), the surface roughness was $16.2 \pm 1.6$ and $12.6 \pm 0.8$ nm, respectively. Tsai et al.[49] observed the same behavior: the increase in roughness with increasing amount of RGO incorporated into $TiO_2$ films is not linear, due to the heterogeneity of the composite films. The AFM images for the $TiO_2$/RGO films also show that a part of the RGO sheets are on the surface of the $TiO_2$ film. We also found other regions in the AFM images where the RGO sheets are decorated with $TiO_2$ nanoparticles. In conclusion, we obtain a heterogeneous mixture between the two components: RGO and $TiO_2$.

KPFM measurements were obtained in the same area of the AFM images to compare the electric potential distribution on the surface of the FTO substrate, $TiO_2$ and $TiO_2$/RGO films.

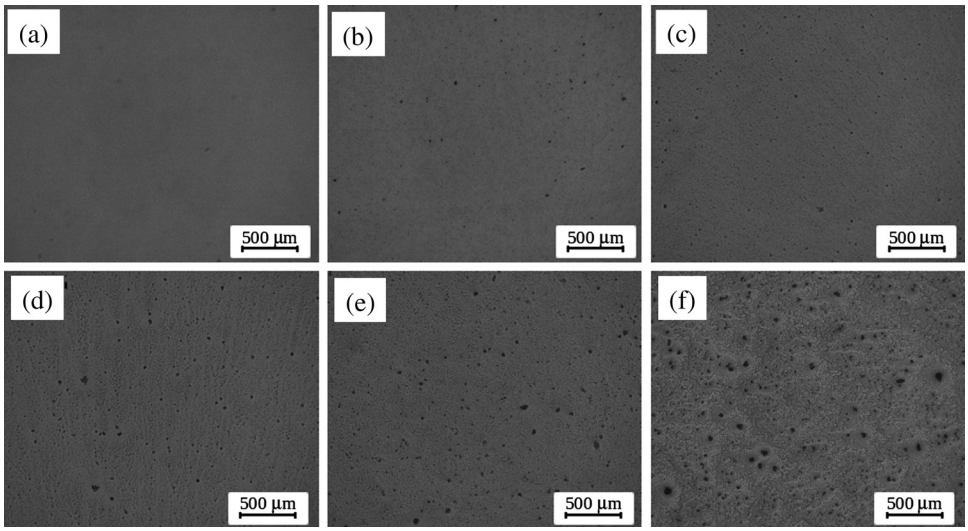


**Fig. 5** Optical microscopy images of the (a) $TiO_2$, (b) $TiO_2$/RGO (0.1 wt%), (c) $TiO_2$/RGO (0.5 wt%), (d) $TiO_2$/RGO (1.0 wt%), (e) $TiO_2$/RGO (2.0 wt%) and (f) $TiO_2$/RGO (4.0 wt%) films.



Downloaded From: http://photonicsforenergy.spiedigitallibrary.org/ on 04/20/2016 Terms of Use: http://spiedigitallibrary.org/ss/TermsOfUse.aspx

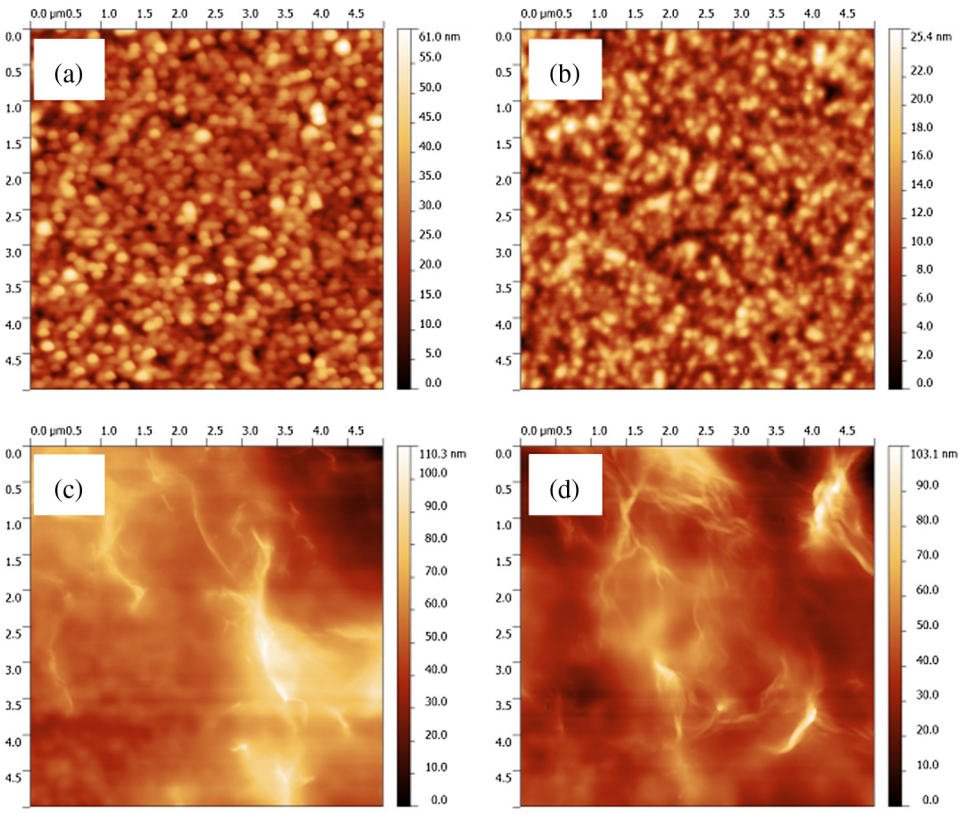


**Fig. 6** AFM images of the (a) FTO substrate, (b) $TiO_2$, (c) $TiO_2$/RGO (2.0 wt%), and (d) $TiO_2$/RGO (4.0 wt%) films.

The voltage profiles of the substrate and films, obtained in $5 \times 5$ $\mu m^2$ sections, are presented in Fig. 7. The average surface potential (SP) values for the FTO substrate, $TiO_2$ and $TiO_2$/RGO films were calculated. The FTO substrate presented a homogeneous electric potential distribution with average SP value of $-0.86$ V. The substrate was used as reference and the relative SP values were obtained for $TiO_2$ and $TiO_2$/RGO films.[50] For the $TiO_2$ films, a homogeneous electric potential distribution with little contrast is found, being the relative SP of $-0.07$ V. The SP of the films after incorporation of RGO (2.0 wt%) increased to 0.18 V, and the potential distribution becomes heterogeneous, allowing a clearer view of regions with different charge densities. The effect observed in $TiO_2$/RGO (4.0 wt%) film is a more positive shift in SP values, however, the electrical potential is a little more homogeneous. The changes in the electrical potential show that after RGO introduction, regions with different charge dissipation capacity were created. In a previous work, we studied $TiO_2$/MWCNT composite films and the variation of SP of the films was attributed to grain boundaries, showing different charge densities between the grains and the interfaces.[51] Even with a substantial difference between the surface roughness of the films containing $TiO_2$ and $TiO_2$/RGO, as demonstrated by AFM images, the change in SP of the $TiO_2$ film after the addition of RGO is significant, indicating that the grains have a relative difference in charge density between themselves and their interfaces.

Liscio et al.[52] demonstrated that introduction of $TiO_2$ nanorods into P3HT film promotes the decrease in SP, improving the charge dissipation in active layers. Under illumination, negative shifts in SP were observed for P3HT/$TiO_2$ bulk heterojunction deposited under ITO/PEDOT:PSS substrates. This fact was attributed to the photogenerated electrons and the hole drift to ITO.[52] In inverted hybrid bulk-heterojunction solar cells using $TiO_2$/reduced GO films, electrons are referred to the FTO substrate. The introduction of reduced GO into $TiO_2$ films promotes a positive shift in SP values. This shift can suggest that electrons are transported to the FTO substrate, while holes remain in the $TiO_2$/RGO surface. Thus, the electron collection capacity can be increased with the addition of RGO.



Downloaded From: http://photonicsforenergy.spiedigitallibrary.org/ on 04/20/2016 Terms of Use: http://spiedigitallibrary.org/ss/TermsOfUse.aspx

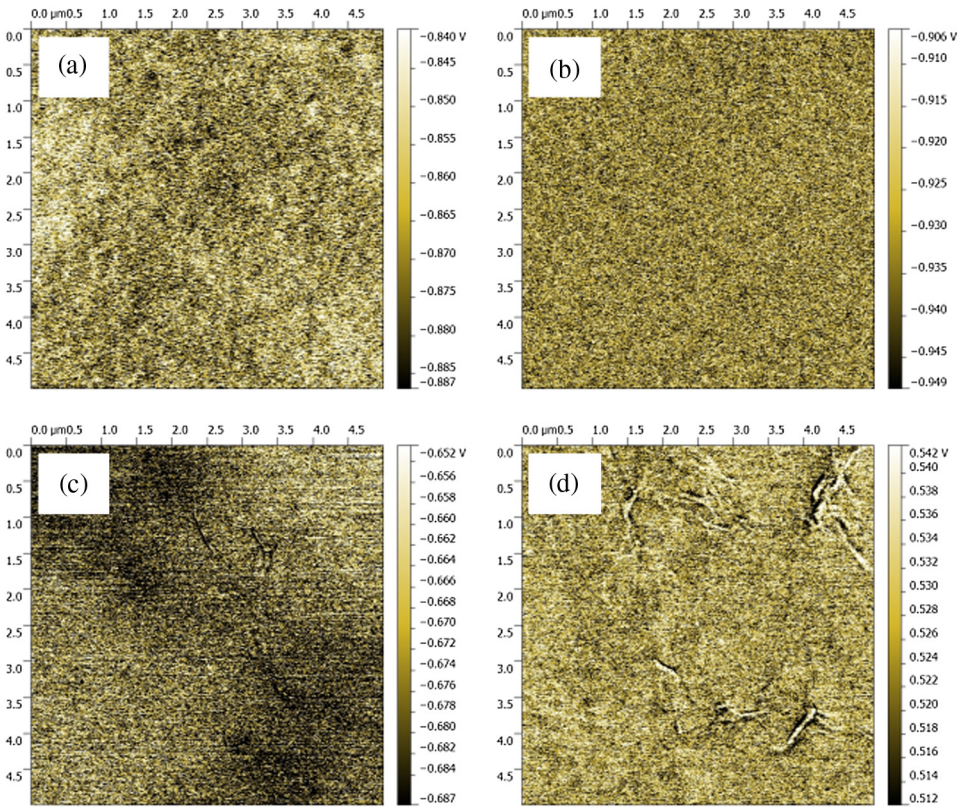


**Fig. 7** KPFM images of the (a) FTO substrate, (b) $TiO_2$ (c) $TiO_2$/RGO (2.0 wt%), and (d) $TiO_2$/RGO (4.0 wt%) films.

Figure 8 shows the UV-visible absorption spectra of the $TiO_2$ and $TiO_2$/RGO films. A significant increase in the absorption at wavelengths shorter than 400 nm is assigned to the intrinsic band gap absorption of the titanium oxide (~3.2 eV).[53] The presence of RGO significantly affects the light absorption in all $TiO_2$/RGO films. Films with higher amounts of RGO resulted in darker films showing an increase in light adsorption within the investigated region. This behavior will have an important implication in the efficiency of photovoltaic devices, as will be discussed in the next section.

### 3.3 *Photovoltaic Performance of the Devices*

The inverted hybrid bulk-heterojunction solar cells (FTO|$TiO_2$ or $TiO_2$/RGO|P3HT:$PC_{61}BM$|$V_2O_5$|Ag) were characterized using $J$–$V$ curves obtained under illumination

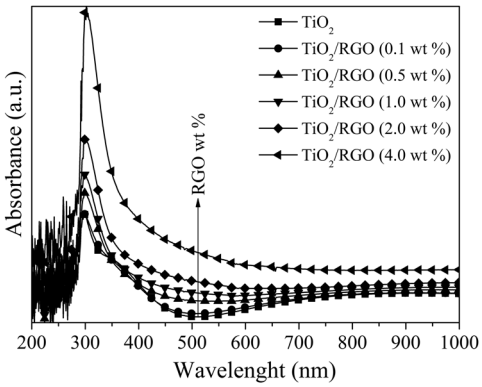


**Fig. 8** UV-vis absorption spectra for the thin $TiO_2$/RGO films.



Downloaded From: http://photonicsforenergy.spiedigitallibrary.org/ on 04/20/2016 Terms of Use: http://spiedigitallibrary.org/ss/TermsOfUse.aspx

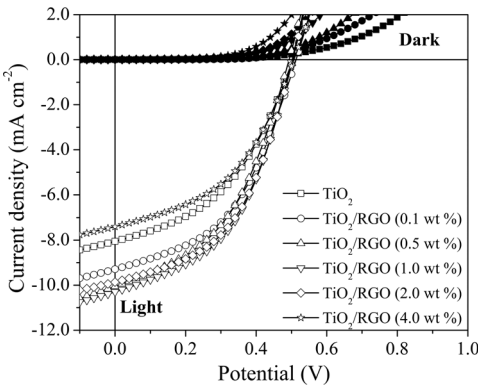


**Fig. 9** $J-V$ curves for the inverted hybrid bulk-heterojunction solar cells (FTO|$TiO_2$ or $TiO_2$/RGO|P3HT:$PC_{61}BM$|$V_2O_5$|Ag) using $TiO_2$, $TiO_2$/RGO (0.1 wt%), $TiO_2$/RGO (0.5 wt%), $TiO_2$/RGO (1.0 wt%), $TiO_2$/RGO(2.0 wt%), and $TiO_2$/RGO (4.0 wt%) films as ETL; under illumination (100 mW cm$^{-2}$, AM 1.5G) and dark conditions. Active cell area: 0.17 cm$^{-2}$.

(100 mW cm$^{-2}$, AM 1.5G) and dark conditions. The effect of incorporation of different amounts of RGO into the $TiO_2$ film was studied and the results are shown in Fig. 9.

The performance of the devices was dependent on the concentration of RGO incorporated into $TiO_2$ films. The $J$–$V$ curves show that at low concentrations of RGO (<2.0 wt%), there was a marked increase in the short circuit current density ($J_{sc}$) and fill factor (FF) values. Noticeably, there was only a small difference between the results with the $TiO_2$/RGO films containing 0.1, 0.5, 1.0, and 2.0 wt% of RGO. However, a dramatic decrease in performance was observed using $TiO_2$ films containing a higher concentration of RGO (4.0 wt%). In this case, the increased charge recombination was one of the main factors of the decline in the efficiency of these devices and this effect can also be evidenced by observing the $J$–$V$ curves in the dark (Fig. 9).

For the investigation of the effect of the RGO concentration in the $TiO_2$ film, seven different devices ($n = 7$) for each concentration of RGO were assembled and then the average and standard deviation of the results were obtained. Table 1 shows the photovoltaic parameters short circuit current density ($J_{sc}$), open circuit potential ($V_{oc}$), FF, PCE, series resistance ($R_s$), and shunt resistance ($R_{sh}$), calculated from the $J$–$V$ curves obtained in the inverted solar cells using $TiO_2$ films with different concentrations of RGO as ETL. Graphs for all photovoltaic parameters ($J_{sc}$, $V_{oc}$, FF, PCE, $R_s$, and $R_{sh}$) were constructed with their respective average and standard deviation versus the concentration of RGO in the $TiO_2$ film shown in Fig. 10.

As shown in Table 1, when the concentration of RGO increases from 0 to 2.0 wt% in the $TiO_2$ film, the average $J_{sc}$ increases from 7.94 to 9.71 mA cm$^{-2}$, and then decreases to 7.41 mA cm$^{-2}$ when the amount of RGO is further increased (4.0 wt%). This behavior is apparent in Fig. 10(a),

**Table 1** Photovoltaic parameters obtained for inverted hybrid bulk-heterojunction solar cells (FTO|$TiO_2$ or $TiO_2$/RGO|P3HT:$PC_{61}BM$|$V_2O_5$|Ag) using $TiO_2$, $TiO_2$/RGO (0.1 wt%), $TiO_2$/RGO (0.5 wt %), $TiO_2$/RGO (1.0 wt %), $TiO_2$/RGO (2.0 wt %), and $TiO_2$/RGO (4.0 wt %) films as ETL. Active cell area: 0.17 cm$^{-2}$.

| Films | $J_{sc}$ (mA cm$^{-2}$) | $V_{oc}$ (V) | FF (%) | PCE (%) | $R_s$ ($10^5$ Ω) | $R_{sh}$ ($10^5$ Ω) |
|---|---|---|---|---|---|---|
| $TiO_2$ | 7.94 ± 0.66 | 0.51 ± 0.01 | 44.0 ± 1.22 | 1.80 ± 0.18 | 1.39 ± 0.34 | 1.15 ± 0.16 |
| $TiO_2$/RGO (0.1 wt%) | 9.43 ± 0.16 | 0.51 ± 0.01 | 45.5 ± 1.39 | 2.20 ± 0.13 | 1.16 ± 0.08 | 1.27 ± 0.17 |
| $TiO_2$/RGO (0.5 wt%) | 9.59 ± 0.58 | 0.50 ± 0.01 | 45.4 ± 0.56 | 2.19 ± 0.11 | 1.11 ± 0.05 | 1.28 ± 0.09 |
| $TiO_2$/RGO (1.0 wt%) | 9.49 ± 0.61 | 0.51 ± 0.01 | 46.0 ± 1.39 | 2.22 ± 0.12 | 1.13 ± 0.11 | 1.33 ± 0.10 |
| $TiO_2$/RGO (2.0 wt%) | 9.71 ± 0.50 | 0.51 ± 0.01 | 47.4 ± 2.26 | 2.32 ± 0.07 | 1.02 ± 0.12 | 1.38 ± 0.15 |
| $TiO_2$/RGO (4.0 wt%) | 7.41 ± 0.58 | 0.51 ± 0.01 | 42.4 ± 3.25 | 1.58 ± 0.14 | 1.66 ± 0.28 | 1.38 ± 0.15 |



Downloaded From: http://photonicsforenergy.spiedigitallibrary.org/ on 04/20/2016 Terms of Use: http://spiedigitallibrary.org/ss/TermsOfUse.aspx

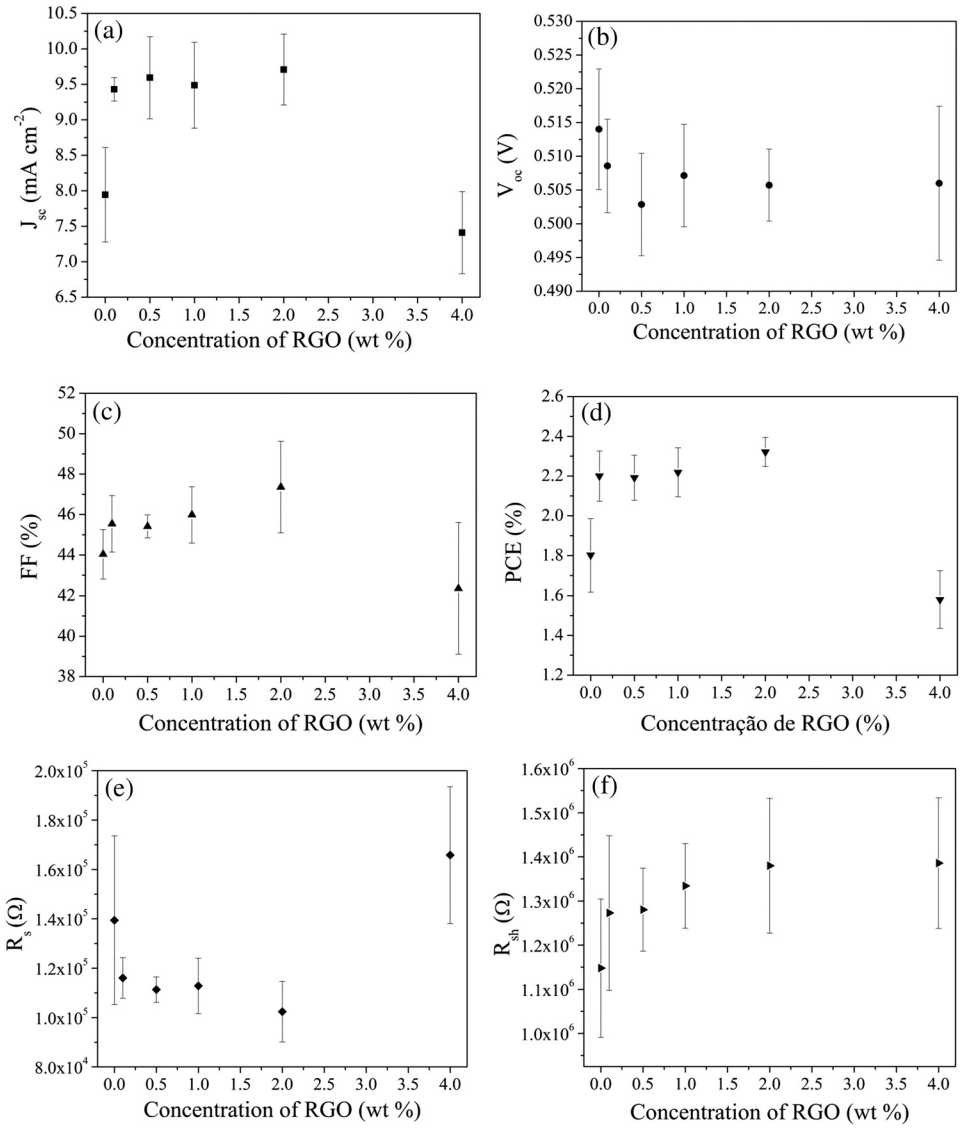


**Fig. 10** Variation of the photovoltaic parameters obtained for inverted hybrid bulk-heterojunction solar cells using $TiO_2$ films with different RGO concentration. (a) $J_{sc}$, (b) $V_{oc}$, (c) FF, (d) PCE, (e) $R_s$ e (f) $R_{sh}$. Configuration: FTO|$TiO_2$ or $TiO_2$/RGO|P3HT:$PC_{61}$BM|$V_2O_5$|Ag. Active cell area: 0.17 cm$^{-2}$.

which represents a graph of the variation of $J_{sc}$ versus the concentration of RGO. Thus, the $TiO_2$/RGO (2.0 wt%) film showed a 22.3% higher average $J_{sc}$ compared to the $TiO_2$ film, followed by a decrease of 23.7% when using the $TiO_2$/RGO film (4.0 wt%). There was no significant difference in the average $J_{sc}$ values between the $TiO_2$/RGO films containing 0.1, 0.5, 1.0 and 2.0 wt% of RGO. We propose that a low concentration of RGO (<2.0 wt%) is sufficient to introduce an alternative conduction pathway, which facilitates a rapid electron transport in the $TiO_2$ films, as suggested from KPFM images (Fig. 7). A similar behavior was observed by Lee et al.[13] who proposed the use of ZnO:RGO films to act as ETL in inverted solar cells using the following configuration: ITO|ZnO:RGO|P3HT:$PC_{61}$BM|PEDOT:PSS|Ag. The study reported that the increase in $J_{sc}$ is related to the increase in conductivity of the film and reduction of the interfacial resistance between the composite film and the active layer, evidenced in electrochemical impedance measurements. In this case, due to its conductive properties, the RGO sheets can also act as an electron collector in the $TiO_2$ film, resulting in an increase in photocurrent and conversion efficiency. We also propose that a higher concentration of RGO (4.0 wt%) promotes an increase of the light absorption due to film darkening, as shown in



Downloaded From: http://photonicsforenergy.spiedigitallibrary.org/ on 04/20/2016 Terms of Use: http://spiedigitallibrary.org/ss/TermsOfUse.aspx

Fig. 8, and agglomerations of RGO sheets are observed in Fig. 5(f). These factors caused a marked decrease of $J_{sc}$ and, therefore, a decrease in the performance of the devices.

Figure 10(b) shows that the average $V_{oc}$ values did not vary significantly with increasing concentration of RGO, remaining almost constant around 0.51 V. On the other hand, there was a relative increase in average FF values due to the presence of RGO, with only the $TiO_2$/RGO (4.0 wt%) film showing a drop. Figure 10(c) shows a relative increase of 7.7% in the FF of the $TiO_2$/RGO (2.0 wt%) film compared to the $TiO_2$ film. The decrease in FF to 42.4% in the $TiO_2$/RGO (4.0 wt%) films is directly related to the increase in the $R_s$ ($1.66 \times 10^5$ Ω) as shown in Fig. 10(e). The addition of RGO can reduce the $R_s$ between the FTO and active layer, promoting efficient electron transfer to the electrodes. For higher amounts of RGO, an increase in $R_s$ was observed due to the large resistance toward out-of-the plane conduction among RGO sheets.[54,55] The $TiO_2$/RGO film thickness (see in Fig. 13 in Appendix) is also a determining factor for a solar cell. In this case, for thick $TiO_2$/RGO films, the electron transport path becomes longer and, therefore, there is an increased probability of charge recombination. Because of this, the $R_s$ values may be relatively high. Regarding the $R_{sh}$ values plotted in Fig. 10(f), there was a small increase in these values with the incorporation of RGO in the $TiO_2$ film. These factors directly affect the PCE of these devices, which when combined caused an improvement from 1.80 to 2.32% with the addition of RGO (0 to 2.0 wt%) and a reduction to 1.58% with the $TiO_2$/RGO (4.0 wt%) film.

To understand the different photocurrent characteristics of inverted solar cells fabricated with $TiO_2$/RGO films, the IPCE spectra as a function of wavelength from 300 to 800 nm were collected. Figure 11 represents the IPCE spectra obtained for the devices (FTO|$TiO_2$ or $TiO_2$/RGO|P3HT:$PC_{61}BM$|$V_2O_5$|Ag) using $TiO_2$ films containing different concentrations of RGO as ETL.

According to the IPCE spectra (Fig. 11), a maximum at 520 nm for all analyzed devices was observed, which related to the wavelength where the P3HT polymer has a maximum absorption.[56] The IPCE spectra display a clear increase in IPCE with a higher RGO content in the $TiO_2$ film. The largest IPCE is seen for the device assembled with $TiO_2$/RGO (1.0 wt%) and $TiO_2$/RGO (2.0 wt%) film due to the increased conductivity and decrease of $R_s$ [see Fig. 10(e)]. Therefore, this device has a maximum IPCE around 49.3%, which is 18.2% higher than in the pristine $TiO_2$ film [$IPCE_{(520\,nm)} \sim 41.7\%$]. Other films such as $TiO_2$/RGO (0.1 wt%) and $TiO_2$/RGO (0.5 wt%) showed maximum IPCE values in the region near 520 nm around 45.1% and 48.3%, respectively. By contrast, the $TiO_2$/RGO (4.0 wt%) film showed a maximum IPCE of 38.4% due to the increased $R_s$ [see Fig. 10(e)], resulting in an increase of charge recombination and a decrease in the performance of these devices. The integrated photocurrent based on the IPCE data is in agreement with the photocurrent data [Fig. 10(a)] measured using the solar simulator, with an error of about 10% (see in Table 5 in Appendix).

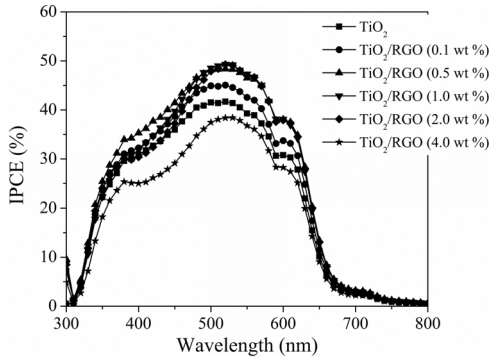


**Fig. 11** IPCE spectra for inverted hybrid bulk-heterojunction solar cells (FTO|$TiO_2$ or $TiO_2$/RGO|P3HT:$PC_{61}BM$|$V_2O_5$|Ag) using $TiO_2$, $TiO_2$/RGO (0.1 wt%), $TiO_2$/RGO (0.5 wt%), $TiO_2$/RGO (1.0 wt%), $TiO_2$/RGO (2.0 wt%), and $TiO_2$/RGO (4.0 wt%) films as ETL. Active cell area: 0.17 $cm^{-2}$.



Downloaded From: http://photonicsforenergy.spiedigitallibrary.org/ on 04/20/2016 Terms of Use: http://spiedigitallibrary.org/ss/TermsOfUse.aspx

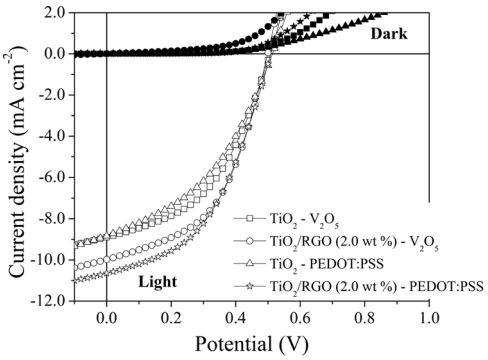


**Fig. 12** $J-V$ curves for the inverted hybrid bulk-heterojunction solar cells (FTO|$TiO_2$ or $TiO_2$/RGO (2.0 wt%)|P3HT:$PC_{61}BM$|$V_2O_5$ or PEDOT:PSS|Ag) using $TiO_2$ or $TiO_2$/RGO (2.0 wt%) films as ETL, under illumination (100 mW cm$^{-2}$, AM 1.5G) and dark conditions. Active cell area: 0.17 cm$^{-2}$.

**Table 2** Photovoltaic parameters obtained for inverted hybrid bulk-heterojunction solar cells (FTO|$TiO_2$ or $TiO_2$/RGO|P3HT:$PC_{61}BM$|$V_2O_5$ or PEDOT:PSS|Ag) using $TiO_2$ or $TiO_2$/RGO (2.0 wt%) films as ETL. Active cell area: 0.17 cm$^{-2}$.

| Films | HTL | $J_{sc}$ (mA cm$^{-2}$) | $V_{oc}$ (V) | FF (%) | PCE (%) | $R_s$ ($10^5$ Ω) | $R_{sh}$ ($10^6$ Ω) |
|---|---|---|---|---|---|---|---|
| $TiO_2$ | $V_2O_5$ | 8.89 | 0.51 | 45.8 | 2.06 | 1.07 | 1.35 |
| $TiO_2$/RGO (2.0 wt%) | $V_2O_5$ | 9.98 | 0.51 | 49.2 | 2.45 | 0.82 | 1.29 |
| $TiO_2$ | PEDOT:PSS | 8.83 | 0.51 | 41.2 | 1.87 | 1.46 | 1.05 |
| $TiO_2$/RGO (2.0 wt%) | PEDOT:PSS | 10.65 | 0.51 | 46.0 | 2.49 | 1.06 | 1.51 |

The proposal of using thin $V_2O_5$ films as HTL is because of its higher stability to the ambient atmosphere relative to PEDOT:PSS, which has been shown to be detrimental for organic solar cells due to its high hygroscopic capacity and its acidic pH Ref. 35. The best results obtained by inverted solar cells using $TiO_2$ or $TiO_2$/RGO (2.0 wt%) as ETL and $V_2O_5$ or PEDOT:PSS as HTL are shown in Fig. 12. This study aimed to compare the photovoltaic behavior between the devices based on $V_2O_5$ and PEDOT:PSS as HTL.

In general, the photovoltaic behavior is relatively similar between the devices with configuration FTO|$TiO_2$|P3HT:$PC_{61}BM$|$V_2O_5$ or PEDOT:PSS|Ag and between FTO|$TiO_2$/RGO(2.0 wt%)|P3HT:$PC_{61}BM$|$V_2O_5$ or PEDOT:PSS|Ag. Table 2 shows the photovoltaic parameters such as $J_{sc}$, $V_{oc}$, FF, PCE, $R_s$ e $R_{sh}$, calculated from the $J$–$V$ curves obtained for the best inverted solar cells using $TiO_2$ and $TiO_2$/RGO (2.0 wt%) films as ETL and $V_2O_5$ or PEDOT:PSS as HTL.

According to Table 2, the inverted solar cells based on $TiO_2$/RGO (2.0 wt%) film, for both configurations, using $V_2O_5$ or PEDOT:PSS as HTL, showed an increase in $J_{sc}$, FF e PCE and a decrease in $R_s$, compared to the devices based on the pure $TiO_2$ film. The $TiO_2$/RGO (2.0 wt%) film showed an increase of 18.9% in PCE when using $V_2O_5$ as HTL and an increase of 33.1% using PEDOT:PSS as HTL. Therefore, independent of the use of $V_2O_5$ or PEDOT: PSS films as HTL, the incorporation 2.0 wt% of RGO into $TiO_2$ films had a positive impact, showing that the RGO sheets can introduce an alternative conduction pathway which facilitates the electron transport.

## 4 Conclusions

In this work, we developed $TiO_2$/RGO films obtained from a sol-gel method, employing $Ti(O^i Pr)_4$ and GO as the starting materials. These films were used as ETL in inverted hybrid



Downloaded From: http://photonicsforenergy.spiedigitallibrary.org/ on 04/20/2016 Terms of Use: http://spiedigitallibrary.org/ss/TermsOfUse.aspx

bulk-heterojunction solar cells. In the photovoltaic studies, the influence of different amounts of RGO in the $TiO_2$ film was investigated and compared to pristine $TiO_2$ films. The best solar cells based on the $TiO_2$/RGO films were obtained when the amount of RGO was 2.0 wt%. Devices based on the $TiO_2$/RGO (2.0 wt%) films exhibited a $J_{sc}$ and PCE of 9.71 mA $cm^{-2}$ and 2.32%, an enhancement of ~22.3% and ~28.9%, respectively, when compared with devices based on pristine $TiO_2$ films. Independent of the use of $V_2O_5$ or PEDOT:PSS films as HTL, the incorporation 2.0 wt% of RGO into $TiO_2$ films had a positive impact. The presence of RGO promotes the formation of regions with higher electron collection capacity and reduced Schottky barrier, providing devices with better performances due to more efficient electron transport to the electrodes, as suggested from KPFM images and $R_s$ values. In general, because of its conductive properties, the RGO sheets can act as an electron collector in the $TiO_2$ film, resulting in an increase in photocurrent and conversion efficiency. However, a dramatic decrease in performance was observed using $TiO_2$/RGO (4.0 wt%) films due to the increase of $R_s$, caused by increased resistance toward out-of-plane conduction among RGO sheets and the film darkening, reducing the light absorption of the active layer.

## Appendix

The thickness of the $TiO_2$ and $TiO_2$/RGO films was estimated through the cross-section of SEM images of all the films, as presented in Fig. 13(a). Figure 13(b) illustrates a graph relating thickness variation versus the concentration of RGO (wt%) for each film.

Figure 13(b) shows that the film's thickness increased significantly from 32.2 to 58.5 nm when the concentration of RGO ranged from zero to 1.0 wt%. In higher RGO concentrations, the thickness did not change much. The $TiO_2$/RGO (4.0 wt%) film, for example, had a thickness of about 61 nm, which is relatively close to the value measured for the $TiO_2$/RGO (1.0 wt%) film (~58.3 nm). The increased thickness of the films may be directly related to increased viscosity of the $TiO_2$ dispersions due to addition of GO.

Thermogravimetric analysis (Fig. 14) was performed to investigate all the thermal decomposition steps involved for the sample of lyophilized GO. This sample has low thermal stability and is thermally decomposed after three steps. The first mass loss during the initial heating (100°C) refers to the removal of water molecules trapped between the sheets. The second mass loss is observed at about 170°C with a considerable mass loss (~25%) assigned to the pyrolysis of the labile oxygen-containing functional groups. The major mass loss (~40%) occurs in a temperature range from 530°C to 630°C, which was attributed to the combustion of the carbon skeleton of GO.

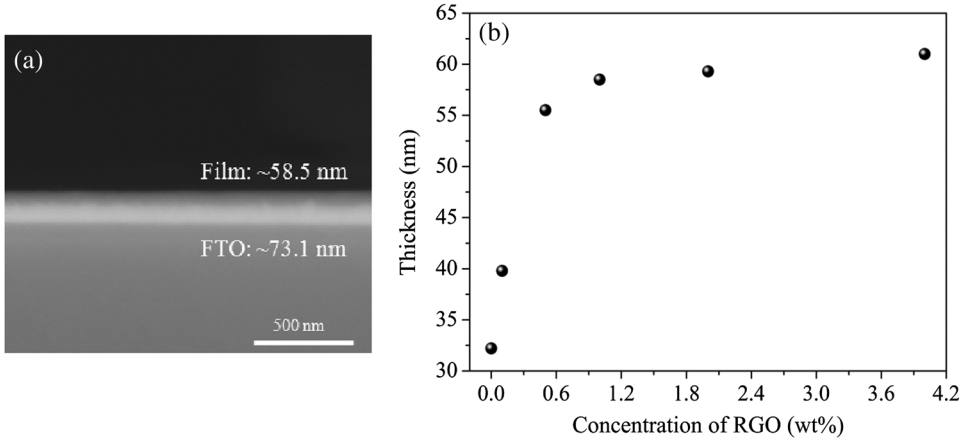


**Fig. 13** (a) Cross-section SEM image of the $TiO_2$/RGO (1.0 wt%) film. (b) Graph of the estimated thickness versus RGO concentration (wt%) for each film.



Downloaded From: http://photonicsforenergy.spiedigitallibrary.org/ on 04/20/2016 Terms of Use: http://spiedigitallibrary.org/ss/TermsOfUse.aspx

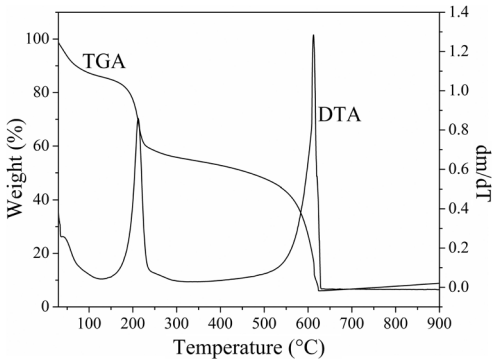


**Fig. 14** TGA-DTA curves for the sample of lyophilized graphene oxide in synthetic air.

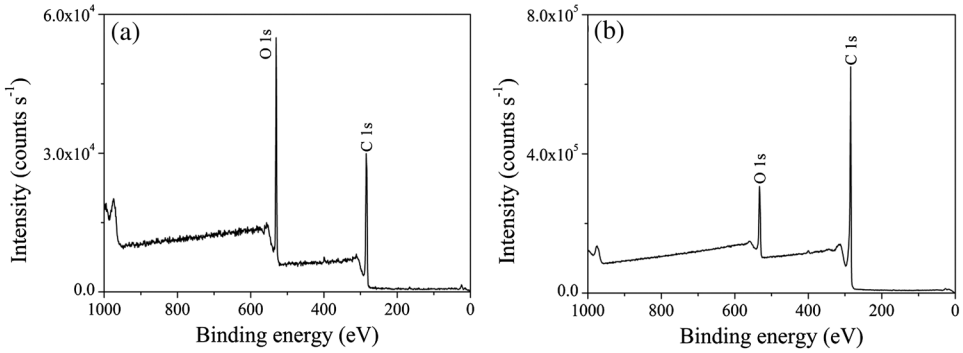


**Fig. 15** XPS survey spectra for samples of (a) GO and (b) RGO films, showing the chemical elements in each sample.

XPS survey spectra (up to 1000 eV) were obtained to identify and quantify the elements and chemical groups present in the GO and RGO films, as shown in Fig. 15. The spectra essentially showed the presence of the elements: carbon (C 1s) and oxygen (O 1s) in the region around 284 eV and 532 eV, respectively. Table 3 shows the values of the binding energies, atomic percentage (at %) and the full width at half maximum (FWHM) obtained from each XPS survey spectrum corresponding to the predominant chemical elements carbon and oxygen. According to these data, the C/O ratio was 2.0 for the GO film. This is an indication that functional groups containing oxygen were introduced in the pristine graphite after the oxidation process. For the sample of RGO film, the C/O ratio was 5.8, showing that there was a small increase in this ratio due to partial removal of functional groups containing oxygen after the thermal treatment at 350°C for 1 h.

**Table 3** Summary of the XPS binding energies, FWHM (in eV) and atomic percentages for the chemical elements found in GO and RGO films with content higher than 1 at %.

| Sample | Element | Binding energy (eV) | FWHM | at % |
|---|---|---|---|---|
| GO film | C | 284.6 | 2.9 | 67.0 |
| | O | 532.6 | 4.3 | 33.0 |
| RGO film (350°C for 1 h) | C | 284.6 | 3.0 | 85.2 |
| | O | 532.6 | 4.2 | 14.8 |



Downloaded From: http://photonicsforenergy.spiedigitallibrary.org/ on 04/20/2016 Terms of Use: http://spiedigitallibrary.org/ss/TermsOfUse.aspx

**Table 4** Sumary of XPS C1s data obtained from fitting calculations regarding the binding energy values, full width at half maximum (FWHM), percentage of each component, and their respective assignments.

| Samples | Assignments | Binding energy (eV) | FWHM | at % |
|---|---|---|---|---|
| GO film | C=C | 284.2 | 1.2 | 32.1 |
| | C–C | 284.9 | 0.9 | 13.6 |
| | C–OH | 285.5 | 0.5 | 3.7 |
| | C–O–C | 286.4 | 1.2 | 42.4 |
| | C=O | 287.7 | 1.1 | 5.5 |
| | O–C=O | 288.7 | 1.0 | 2.2 |
| | $\pi-\pi^*$ | 289.8 | 0.5 | 0.5 |
| RGO film (350°C for 1 h) | C=C | 284.2 | 0.9 | 53.1 |
| | C–C | 284.9 | 0.9 | 12.2 |
| | C–OH | 285.4 | 1.6 | 14.5 |
| | C–O–C | 286.1 | 1.3 | 9.9 |
| | C=O | 287.4 | 1.9 | 8.5 |
| | O–C=O | 288.7 | 0.8 | 1.5 |
| | $\pi-\pi^*$ | 290.1 | 0.6 | 0.3 |

**Table 5** Short circuit current density ($J_{sc}$) measured using the solar simulator and its theoretical value calculated by integrating the IPCE spectra.

| Films | $J_{sc}$ (mA cm$^{-2}$) measured using the solar simulator | $J_{sc}$ (mA cm$^{-2}$) theoretical value calculated by integrating the IPCE spectra |
|---|---|---|
| $TiO_2$ | 8.05 | 9.27 |
| $TiO_2$/RGO (0.1 wt%) | 9.29 | 10.01 |
| $TiO_2$/RGO (0.5 wt%) | 10.05 | 11.03 |
| $TiO_2$/RGO (1.0 wt%) | 10.29 | 10.88 |
| $TiO_2$/RGO (2.0 wt%) | 9.86 | 10.75 |
| $TiO_2$/RGO (4.0 wt%) | 7.40 | 8.24 |

## Acknowledgments

The authors thank LNNano/LNLS for the AFM and KPFM images, and INEO, CNPq (fellowship 246430/2012-5), and FAPESP (fellowship 2010/18656-1) for the financial supports. The authors would like to thank Dr. Emre Yassitepe for the XPS measurements at LNNano/LNLS. The authors are also indebted to MSc. Nicolau Saker Neto for manuscript revision. MINECO for the economic support through the ENE2013-48816-C5-4-R project. The COST Action StableNextSol project MP1307. The Agència de Gestió d'Ajuts Universitaris i de Recerca for the project 2014 SGR 1212. FASL would like to thank to the Secretary of Education of the State of Ceará (SEDUC-CE) for the financial support.



Downloaded From: http://photonicsforenergy.spiedigitallibrary.org/ on 04/20/2016 Terms of Use: http://spiedigitallibrary.org/ss/TermsOfUse.aspx

## References


1. S. K. Hau, H. L. Yip, and A. K. Y. Jen, "A review on the development of the inverted polymer solar cell architecture," *Polym. Rev.* **50**(4), 474–510 (2010).
2. Y. Y. Liang et al., "For the bright future-bulk heterojunction polymer solar cells with power conversion efficiency of 7.4%," *Adv. Mater.* **22**(20), E135–E138 (2010).
3. S. J. Liu et al., "High-efficiency polymer solar cells via the incorporation of an amino-functionalized conjugated metallopolymer as a cathode interlayer," *J. Am. Chem. Soc.* **135**(41), 15326–15329 (2013).
4. C. Cabanetos et al., "Linear side chains in benzo[1,2-b:4,5-b′]dithiophene-thieno[3,4-c]pyrrole-4,6-dione polymers direct self-assembly and solar cell performance," *J. Am. Chem. Soc.* **135**(12), 4656–4659 (2013).
5. K. S. Yeo et al., "Application of sputter-deposited amorphous and anatase $TiO_2$ as electron-collecting layers in inverted organic photovoltaics," *Org. Electron.* **14**(7), 1715–1719 (2013).
6. I. Sasajima et al., "Flexible inverted polymer solar cells containing an amorphous titanium oxide electron collection electrode," *Org. Electron.* **12**(1), 113–118 (2011).
7. D. R. Bekci and S. Erten-Ela, "Effect of nanostructured ZnO cathode layer on the photovoltaic performance of inverted bulk heterojunction solar cells," *Renewable Energy* **43**, 378–382 (2012).
8. L. K. Jagadamma et al., "Efficient inverted bulk-heterojunction solar cells from low-temperature processing of amorphous ZnO buffer layers," *J. Mater. Chem. A* **2**(33), 13321–13331 (2014).
9. H. Y. Sun et al., "UV light protection through $TiO_2$ blocking layers for inverted organic solar cells," *Sol. Energy Mater. Sol. C* **95**(12), 3450–3454 (2011).
10. H. Zhang et al., "Enhanced performance of inverted organic photovoltaic cells using CNTs-$TiO_x$ nanocomposites as electron injection layer," *Nanotechnology* **24**(35), 355401 (2013).
11. Y. Zhang et al., "Enhanced electron collection in inverted organic solar cells using titanium oxide/reduced graphene oxide composite films as electron collecting layers," *Electrochim. Acta* **117**, 438–442 (2014).
12. Y. Zhang, S. Yuan, and W. Liu, "Inverted organic solar cells employing RGO/$TiO_x$ composite films as electron transport layers," *Electrochim. Acta* **143**, 18–22 (2014).
13. H. W. Lee et al., "Highly efficient inverted polymer solar cells with reduced graphene-oxide-zinc-oxide nanocomposites buffer layer," *Appl. Phys. Lett.* **102**(19), 193903 (2013).
14. Q. J. Xiang, J. G. Yu, and M. Jaroniec, "Graphene-based semiconductor photocatalysts," *Chem. Soc. Rev.* **41**(2), 782–796 (2012).
15. X. S. Li et al., "Graphene films with large domain size by a two-step chemical vapor deposition process," *Nano Lett.* **10**(11), 4328–4334 (2010).
16. J. Hass, W. A. de Heer, and E. H. Conrad, "The growth and morphology of epitaxial multilayer graphene," *J. Phys. Condens. Matter* **20**(32), 323202 (2008).
17. F. Chen et al., "Electrochemical gate-controlled charge transport in graphene in ionic liquid and aqueous solution," *J. Am. Chem. Soc.* **131**(29), 9908–9909 (2009).
18. D. Li et al., "Processable aqueous dispersions of graphene nanosheets," *Nat. Nanotechnol.* **3**(2), 101–105 (2008).
19. S. F. Pei and H. M. Cheng, "The reduction of graphene oxide," *Carbon* **50**(9), 3210–3228 (2012).
20. S. Stankovich et al., "Stable aqueous dispersions of graphitic nanoplatelets via the reduction of exfoliated graphite oxide in the presence of poly(sodium 4-styrenesulfonate)," *J. Mater. Chem.* **16**(2), 155–158 (2006).
21. K. Jasuja et al., "Microwave-reduced uncapped metal nanoparticles on graphene: tuning catalytic, electrical, and Raman properties," *J. Phys. Chem. Lett.* **1**(12), 1853–1860 (2010).
22. I. A. Aksay et al., "Single sheet functionalized graphene by oxidation and thermal expansion of graphite," *Chem. Mater.* **19**(18), 4396–4404 (2007).
23. J. N. Ding et al., "The influence of temperature, time and concentration on the dispersion of reduced graphene oxide prepared by hydrothermal reduction," *Diam Relat. Mater.* **21** 11–15 (2012).




Downloaded From: http://photonicsforenergy.spiedigitallibrary.org/ on 04/20/2016 Terms of Use: http://spiedigitallibrary.org/ss/TermsOfUse.aspx

24. L. Chen et al., "Enhanced photovoltaic performance of a dye-sensitized solar cell using graphene-$TiO_2$ photoanode prepared by a novel *in situ* simultaneous reduction-hydrolysis technique," *Nanoscale* **5**(8), 3481–3485 (2013).
25. W. Shu et al., "Synthesis and photovoltaic performance of reduced graphene oxide-$TiO_2$ nanoparticles composites by solvothermal method," *J. Alloy Compd.* **563** 229–233 (2013).
26. F. Y. Pei et al., "$TiO_2$ nanocomposite with reduced graphene oxide through facile blending and its photocatalytic behavior for hydrogen evolution," *Mater. Res. Bull.* **48**(8), 2824–2831 (2013).
27. D. T. Wang et al., "Enhanced photoelectrocatalytic activity of reduced graphene oxide/$TiO_2$ composite films for dye degradation," *Chem. Eng. J.* **198** 547–554 (2012).
28. M. M. Zhen et al., "Well-distributed $TiO_2$ nanocrystals on reduced graphene oxides as high-performance anode materials for lithium ion batteries," *RSC Adv.* **3**(33), 13696–13701 (2013).
29. M. H. Yeh et al., "Dye-sensitized solar cells with reduced graphene oxide as the counter electrode prepared by a green photothermal reduction process," *Chem. Phys. Chem.* **15**(6), 1175–1181 (2014).
30. L. Wan et al., "Room-temperature fabrication of graphene films on variable substrates and its use as counter electrodes for dye-sensitized solar cells," *Solid State Sci.* **13**(2), 468–475 (2011).
31. H. Zhang et al., "Effects of $TiO_2$ film thickness on photovoltaic properties of dye-sensitized solar cell and its enhanced performance by graphene combination," *Mater. Res. Bull.* **49** 126–131 (2014).
32. G. Cheng et al., "Novel preparation of anatase $TiO_2$ at reduced graphene oxide hybrids for high-performance dye-sensitized solar cells," *ACS Appl. Mater. Inter.* **5**(14), 6635–6642 (2013).
33. B. Tang and G. X. Hu, "Two kinds of graphene-based composites for photoanode applying in dye-sensitized solar cell," *J. Power Sources* **220**, 95–102 (2012).
34. N. I. Kovtyukhova et al., "Layer-by-layer assembly of ultrathin composite films from micron-sized graphite oxide sheets and polycations," *Chem. Mater.* **11**(3), 771–778 (1999).
35. G. Teran-Escobar et al., "Low-temperature, solution-processed, layered $V_2O_5$ hydrate as the hole-transport layer for stable organic solar cells," *Energy Environ. Sci.* **6**(10), 3088–3098 (2013).
36. H. Wang and Y. H. Hu, "Effect of oxygen content on structures of graphite oxides," *Ind Eng. Chem. Res.* **50**(10), 6132–6137 (2011).
37. J. F. Shen et al., "One step hydrothermal synthesis of $TiO_2$-reduced graphene oxide sheets," *J. Mater. Chem.* **21**(10), 3415–3421 (2011).
38. A. Kaniyoor and S. Ramaprabhu, "A Raman spectroscopic investigation of graphite oxide derived graphene," *AIP Adv.* **2**(3), 032183 (2012).
39. S. Some et al., "Can commonly used hydrazine produce n-type graphene?," *Chem. Eur. J.* **18**(25), 7665–7670 (2012).
40. S. Stankovich et al., "Synthesis of graphene-based nanosheets via chemical reduction of exfoliated graphite oxide," *Carbon* **45**(7), 1558–1565 (2007).
41. J. F. Shen et al., "Ionic liquid-assisted one-step hydrothermal synthesis of $TiO_2$-reduced graphene oxide composites," *Nano Res.* **4**(8), 795–806 (2011).
42. H. K. Jeong et al., "Thermal stability of graphite oxide," *Chem. Phys. Lett.* **470**(4–6), 255–258 (2009).
43. J. Filik et al., "XPS and laser Raman analysis of hydrogenated amorphous carbon films," *Diamond Relat. Mater.* **12**(3–7), 974–978 (2003).
44. Y. H. Zu et al., "Graphite oxide-supported CaO catalysts for transesterification of soybean oil with methanol," *Bioresour. Technol.* **102**(19), 8939–8944 (2011).
45. H. S. Han et al., "Synthesis of graphene oxide grafted poly(lactic acid) with palladium nanoparticles and its application to serotonin sensing," *Appl. Surf. Sci.* **284** 438–445 (2013).
46. C. Mattevi et al., "Evolution of electrical, chemical, and structural properties of transparent and conducting chemically derived graphene thin films," *Adv. Funct. Mater.* **19**(16), 2577–2583 (2009).




Downloaded From: http://photonicsforenergy.spiedigitallibrary.org/ on 04/20/2016 Terms of Use: http://spiedigitallibrary.org/ss/TermsOfUse.aspx

47. A. Bagri et al., "Structural evolution during the reduction of chemically derived graphene oxide," *Nat. Chem.* **2**(7), 581–587 (2010).
48. D. Yang et al., "Chemical analysis of graphene oxide films after heat and chemical treatments by x-ray photoelectron and micro-Raman spectroscopy," *Carbon* **47**(1), 145–152 (2009).
49. T. H. Tsai, S. C. Chiou, and S. M. Chen, "Enhancement of dye-sensitized solar cells by using graphene-$TiO_2$ composites as photoelectrochemical working electrode," *Int. J. Electrochem. Sci.* **6**(8), 3333–3343 (2011).
50. M. C. Wu et al., "Correlation between nanoscale surface potential and power conversion efficiency of P3HT/$TiO_2$ nanorod bulk heterojunction photovoltaic devices," *Nanoscale* **2**(8), 1448–1454 (2010).
51. A. de Morais et al., "Enhancing in the performance of dye-sensitized solar cells by the incorporation of functionalized multi-walled carbon nanotubes into $TiO_2$ films: The role of MWCNT addition," *J. Photochem. Photobiol. A* **251**, 78–84 (2013).
52. A. Liscio et al., "Photovoltaic charge generation visualized at the nanoscale: a proof of principle," *J. Am. Chem. Soc.* **130**(3), 780 (2008).
53. Q. J. Xiang et al., "Microwave-hydrothermal preparation and visible-light photoactivity of plasmonic photocatalyst Ag-$TiO_2$ nanocomposite hollow spheres," *Chem. Asian J.* **5**(6), 1466–1474 (2010).
54. J. Z. Huang et al., "Incorporation of graphene oxide in quantum dot sensitized photocatalyst based on ZnO nanorods," *J. Nanosci. Nanotechnol.* **14**(4), 3001–3005 (2014).
55. A. K. K. Kyaw et al., "Top-illuminated dye-sensitized solar cells with a room-temperature-processed ZnO photoanode on metal substrates and a Pt-coated Ga-doped ZnO counter electrode," *J. Phys. D Appl. Phys.* **44**(4), 045102 (2011).
56. M. Lira-Cantu et al., "Oxide/polymer interfaces for hybrid and organic solar cells: Anatase vs. Rutile $TiO_2$," *Sol. Energy Mater. Sol. C* **95**(5), 1362–1374 (2011).

**Andreia Morais**, studied at the Federal University of Alfenas-MG (Unifal-MG) and received her degree in chemistry with technological assignments in 2008. She obtained a master's degree in physical chemistry at the Federal University of Alfenas-MG (Unifal-MG) in 2010. Currently, she is pursuing PhD studies in physical chemistry at the State University of Campinas (UNICAMP). Her research focuses on the development of nanostructured composites materials for hydrogen generation from photoelectrochemical water splitting and applications in photovoltaic devices and electrochemical sensors.

**João Paulo C. Alves**, studied at the Federal University of Lavras-MG (UFLA-MG) and received his degree in chemistry in 2009. He obtained a master's degree in inorganic chemistry from the State University of Campinas (UNICAMP), Campinas, Brazil, in 2011. Currently, he is pursuing PhD studies in inorganic chemistry at UNICAMP. His research is based on the development of hybrid polymer–inorganic nanoparticle systems, for applications in photovoltaic devices, and photophysical and morphological studies.

**Francisco Anderson S. Lima**, studied at the State University of Ceará (UFC) and received his degree in physics in 2004. He obtained a master's degree in applied physical sciences at the same State University of Ceará (UFC) in 2010. Currently, he is pursuing PhD studies at the Catalan Institute of Nanoscience and Nanotechnology (ICN2) and at Federal University of Ceará (UFC). His research is devoted to the synthesis, characterization, and application of nanostructured materials for excitonic solar cells.

**Monica Lira-Cantu** received her PhD degree in materials science by the Materials Science Institute of Barcelonas (ICMAB) and Autonoma University of Barcelona in 1997. From 1999 to 2001, she worked as permanent senior staff chemist at ExxonMobil Research and Engineering in New Jersey, USA. Currently, she is a group leader of the nanostructured materials for photovoltaic energy group at the Catalan Institute of Nanoscience and Nanotechnology, ICN2 in Barcelona, Spain. She has coauthored more than 70 published papers, 7 patents, and 8 book chapters, h-index of 26.



Downloaded From: http://photonicsforenergy.spiedigitallibrary.org/ on 04/20/2016 Terms of Use: http://spiedigitallibrary.org/ss/TermsOfUse.aspx

**Ana Flavia Nogueira** received her PhD degree in inorganic chemistry from the UNICAMP in 2001. In 2002, she joined the group of professor James R. Durrant at the Imperial College, London, in a postdoctoral position, where she investigated organic and hybrid solar cells. Since 2004, she has been an associate professor at UNICAMP. She is also the coordinator of the Laboratory of Nanotechnology and Solar Energy, a leading group in the field of third-generation solar cells in Brazil.



Downloaded From: http://photonicsforenergy.spiedigitallibrary.org/ on 04/20/2016 Terms of Use: http://spiedigitallibrary.org/ss/TermsOfUse.aspx